HEALTH AND MEDICINE

Prenatally androgenized PCOS mice have ovary-independent uterine dysfunction and placental inflammation aggravated by high-fat diet

Lena Luyckx[1,2], Milena Myllykangas[1], Ulla Saarela[1], Nikke Virtanen[1], Elisa Hurskainen[1], Audrey Savolainen[3], Nadja Ollikainen[1], Anna-Karin Norlén[4], Claes Ohlsson[5], Matti Poutanen[5,6], Greetje Vande Velde[7], Riikka K. Arffman[1], Renata Prunskaite-Hyyryläinen[3], Joris Vriens[2], Terhi T. Piltonen[1]*

Polycystic ovary syndrome (PCOS) is a common hyperandrogenic and metabolic condition in women. The syndrome is linked to subfertility and pregnancy complications, yet the independent effects of exposure to hyperandrogenism and obesity on endometrial function remain unclear. Here, PCOS-like mice were generated using prenatal androgenization (PNA) with dihydrotestosterone, followed by a prepubertal high-fat (HF) or standard diet. In ovariectomized mice, PNA impaired uterine closure during the implantation window, disrupted decidualization, and altered extracellular matrix– and inflammation-related gene expression. The effects were aggravated by the HF diet. In naturally mated, ovary-intact mice, PNA and HF diet affected decidual and placental gene expression, suggestive of placental dysfunction and inflammation, and induced fetal growth restriction. This study underlines the role of the uterus in adverse pregnancy outcomes in PCOS and identifies possible underlying mechanisms for future studies. Prepregnancy interventions targeting metabolic health and hyperandrogenism should be the next steps to optimize PCOS pregnancy outcomes.

INTRODUCTION

Polycystic ovary syndrome (PCOS) is a common endocrine disorder found in one of eight women with wide reproductive, metabolic, and psychological health implications (*1*). The syndrome is diagnosed by the presence of at least two of the following criteria: irregular menstrual cycles, hyperandrogenism, and polycystic ovarian morphology (*1*). Affected women face up to a 15-fold increased risk of infertility and are also at increased risk for pregnancy complications including miscarriage, preeclampsia, preterm delivery, and small for gestational age (*2*, *3*). While PCOS-related infertility is mainly attributed to ovarian dysfunction and anovulation, the potential contribution of the uterine endometrium to adverse reproductive outcomes has often been overlooked (*4*).

In humans, the monthly menstrual cycle includes the differentiation of the uterine endometrium into a receptive state, a process known as decidualization. This transformation renders the endometrial cells capable of supporting embryo attachment and invasion during the window of implantation (WOI). Successful decidualization also supports normal embryo development, placentation, and successful healthy pregnancy (*5*, *6*). Likewise, decidualization and placentation abnormalities may lead to infertility and pregnancy complications (*4*, *7*).

Women with PCOS commonly experience metabolic disturbances such as long-term obesity, metabolic syndrome, and type 2 diabetes (*1*). Some studies have demonstrated the detrimental effects of high body weight (BW) on endometrial health, as women with obesity are more often anovulatory, have low-grade endometrial inflammation, impaired decidualization, and have poorer outcomes in assisted reproductive technology treatments (*8*). Yet, the precise relationship between obesity and PCOS and their respective contributions to endometrial dysfunction remain elusive (*9*).

Mouse models mimicking PCOS features can be established with the use of prenatal androgenization (PNA). PNA mice exhibit reproductive abnormalities typical for PCOS including disrupted reproductive cycles, increased luteinizing hormone pulse frequency, and ovarian follicle atresia (*10*). A few studies have provided evidence of dysregulated uterine function in PNA animals because PNA rats display increased endometrial androgen receptor (AR) and uterine estrogen receptor β protein expression and hyperplastic morphology (*11*). PNA mice also display aberrant placental gene expression and reduced litter sizes, which may relate to impaired endometrial decidualization (*12*), but the precise underlying mechanisms are not well understood.

Therefore, in this study, we used a PNA-induced PCOS-like mouse model, with or without a high-fat (HF) diet, to study the effects of early-life androgen exposure and excessive BW on uterine endometrial function. We show that PNA causes ovary-independent defects in uterine function during the WOI and decidualization. The HF diet exacerbated these defects in PNA mice, leading to abrupted placental gene expression suggestive of placental dysfunction and inflammation, with subsequent reduction in fetal growth. These insights advance our understanding of PCOS- and obesity-related endometrial pathogenesis and highlight the role of the uterus as a

[1]Department of Obstetrics and Gynecology, Research Unit of Clinical Medicine, Faculty of Medicine, University of Oulu, 90220 Oulu, Finland. [2]Research Group for Implantation, Placentation and Pregnancy, Department of Development and Regeneration, Faculty of Medicine, KU Leuven, 3000 Leuven, Belgium. [3]Protein and Structural Biology Research Unit, Faculty of Biochemistry and Molecular Medicine, University of Oulu, 90220 Oulu, Finland. [4]Department of Clinical Chemistry, Faculty of Medicine, Sahlgrenska University Hospital, 41345 Gothenburg, Sweden. [5]Department of Internal Medicine and Clinical Nutrition, Institute of Medicine, The Sahlgrenska Academy, Gothenburg University, 41345 Gothenburg, Sweden. [6]Research Centre for Integrative Physiology and Pharmacology, Institute of Biomedicine, Faculty of Medicine, University of Turku, 20014 Turku, Finland. [7]Biomedical MRI/MoSAIC, Department of Imaging and Pathology, Faculty of Medicine, KU Leuven, 3000 Leuven, Belgium.
*Corresponding author. Email: terhi.piltonen@oulu.fi

potential target for managing PCOS-related pregnancy complications that seem to be promoted by hyperandrogenism and obesity.

RESULTS

PNA induces PCOS-like phenotype irrespective of BW

To investigate how PNA and HF diet–induced obesity (DIO) affect uterine endometrial function and pregnancy, PNA mice were generated by administering daily injections of 250 μg of dihydrotestosterone (DHT) or vehicle to pregnant dams on gestational days 16.5 to 18.5. From the age of 3 weeks onward, the prepubertal female offspring received an HF diet to enable DIO or a typical laboratory diet. This created four experimental groups depending on PNA status and type of diet: control females receiving typical laboratory diet (CN), PNA females receiving typical laboratory diet (PN), control females with DIO (CHF), and PNA females with DIO (PHF) (Fig. 1A).

The successful induction of the PCOS-like phenotype in PNA mice was confirmed by increased anogenital distance (AGD) (*13*) and disrupted estrous cyclicity (Fig. 1, B to D, and fig. S1A). PNA mice spent less time in estrus and more time in metestrus and diestrus phases compared to controls, and the PHF group showed a prolonged diestrus phase compared to PNA alone (Fig. 1, C and D). Despite these indications supporting successful PCOS-like phenotype establishment, serum testosterone (T) levels at 12 weeks were not different between groups (fig. S1B).

Assessment of the metabolic effects of the HF diet revealed increased weight gain compared to normal diet groups, whereas PNA alone did not affect weight gain (Fig. 1E). CHF and PHF mice also demonstrated increased proportions of white adipose tissue and ovarian fat, and the proportion of brown adipose tissue was increased in CHF mice compared to mice on the normal diet (Fig. 1, F to H). Microcomputed tomography (microCT) analysis showed increased overall abdominal fat and a higher proportion of visceral versus subcutaneous fat in response to the HF diet (Fig. 1I). In addition, fasting blood glucose levels were elevated (Fig. 1J), and homeostatic model assessment for insulin resistance (HOMA-IR) was higher in the PHF group compared to the PN group (Fig. 1K).

PNA alters uterine morphology and gene expression during the WOI

To assess the effects of PNA and DIO on uterine function during the WOI irrespective of ovarian effects, mice were ovariectomized and received estradiol (E2) and progesterone (P4) injections [hormone replacement (HR)] to mimic the hormonal environment of the WOI (Fig. 2A). Similar to physiological conditions, the majority of CN (80%) and 50% of CHF mice demonstrated uterine luminal closure during the WOI, while this was absent in the uteri of all PNA groups (Fig. 2, B and C). Such morphological differences were not observed in uteri from PNA or control mice with intact ovaries during the metestrus phase (fig. S1, C to E).

Next, bulk RNA sequencing (RNA-seq) of the uteri of HR-treated mice revealed major differences in gene expression profiles between PNA and control uteri, as demonstrated by distinct hierarchical clustering (Fig. 2D), Gene Ontology (GO) analysis, and analysis of significantly differentially expressed genes [DEGs; adjusted P (P adj.) < 0.05]. Specifically, pathways and gene expression related to RNA polymerase, ribosome function, and estrogen regulation (*Sprr2f* and *Prap1*) were up-regulated in PN versus CN uteri, suggesting sustained proliferation. Genes involved in endometrial receptivity (*Tdo2* and *Areg*) were also increased, while those related to integrin binding (*Edil3*), extracellular matrix (ECM; *Col28a1* and *Fgf1*), and anion transmembrane activity (*Cftr* and *Ptk2b*) were down-regulated in PN uteri (Fig. 2, E and F).

Comparison of PHF and CHF uteri transcriptomes revealed similarly affected pathways as in PN versus CN uteri, including increased ribosome- and reduced ECM-related pathways in PHF uteri (Fig. 2G). However, a notably higher number of DEGs were found between the PHF and CHF groups (3954) compared to the PN versus CN comparison (40), indicating that diet had a distinct effect in PNA versus control mice. In addition, increased expression of inflammation-associated genes (e.g., *Il17b* and *Il1a*) was found in PHF versus CHF uteri (Fig. 2, G and H). Moreover, the expression of several genes important for endometrial receptivity [*Prap1*, *Itgb3* (*14*), and *Foxo3* (*15*)], steroid hormone receptors (*Ar* and *Esr1*), and genes related to ECM (*Ecm2*, *Col1a1*, *Col3a1*, and Col*28a1*) was reduced in PHF versus CHF uteri (Fig. 2, G and H). While the HF diet alone altered uterine glucose metabolism (elevated *Irs2* and *Txnip* expression), mitochondrial function (reduced *Tomm5* and *Timm23* expression), and phosphatidylinositol 3-kinase (PI3K) pathway–related genes compared to the CN group (fig. S2, A and B), in the PNA group, only three up- and three down-regulated DEGs were observed between PHF and PN mice (fig. S2, C and D).

Reverse transcription quantitative polymerase chain reaction (RT-qPCR) analysis of selected genes (*Col28a1*, *Fgf1*, and *Prap1*) confirmed the expression patterns observed in the RNA-seq data (Fig. 2I). In addition, because many DEGs were related to the ECM, the distribution of collagens was assessed using picrosirius red and Masson's trichrome staining of uterine cross sections. PNA uteri showed an increased optical density (OD) of picrosirius red staining and increased Masson's trichrome staining in the endometrial stroma, both indicating increased collagen deposition in PNA uteri (Fig. 2, J and K, and fig. S2E).

Last, in line with affected pathways and genes related to anion transmembrane transporter activity in PN versus CN uteri (Fig. 2E), a heatmap presenting gene counts of DEGs related to ion channel homeostasis indicated altered expression levels of these genes in PNA groups during the WOI (fig. S2F).

PNA compromises uterine endometrial decidualization, aggravated by the HF diet

To further understand how PNA and DIO affect uterine endometrial function during implantation, the endometrial decidualization process was studied independently of ovarian function by using an established artificial decidualization protocol (*16*). The uteri of ovariectomized mice were hormonally primed with E2 and P4, followed by administering a uterine decidualization stimulus consisting of intrauterine oil injection and mechanical scratching with a blunted needle (Fig. 3A, right horns). The unstimulated uterine horn served as an internal control (Fig. 3A, left horns). Morphological analysis of the isolated uteri revealed that, while all CN and CHF mouse uteri showed a physiological decidualization response, decidualization was achieved in only 42% of PN and 7% of PHF uteri (Fig. 3B). Collagen reorganization was also absent in PNA groups (as shown by picrosirius red staining; Fig. 3B), and the weights of the injected horns were reduced compared to controls (Fig. 3C). The combination of PNA and HF diet reduced uterine weight even further (Fig. 3C).

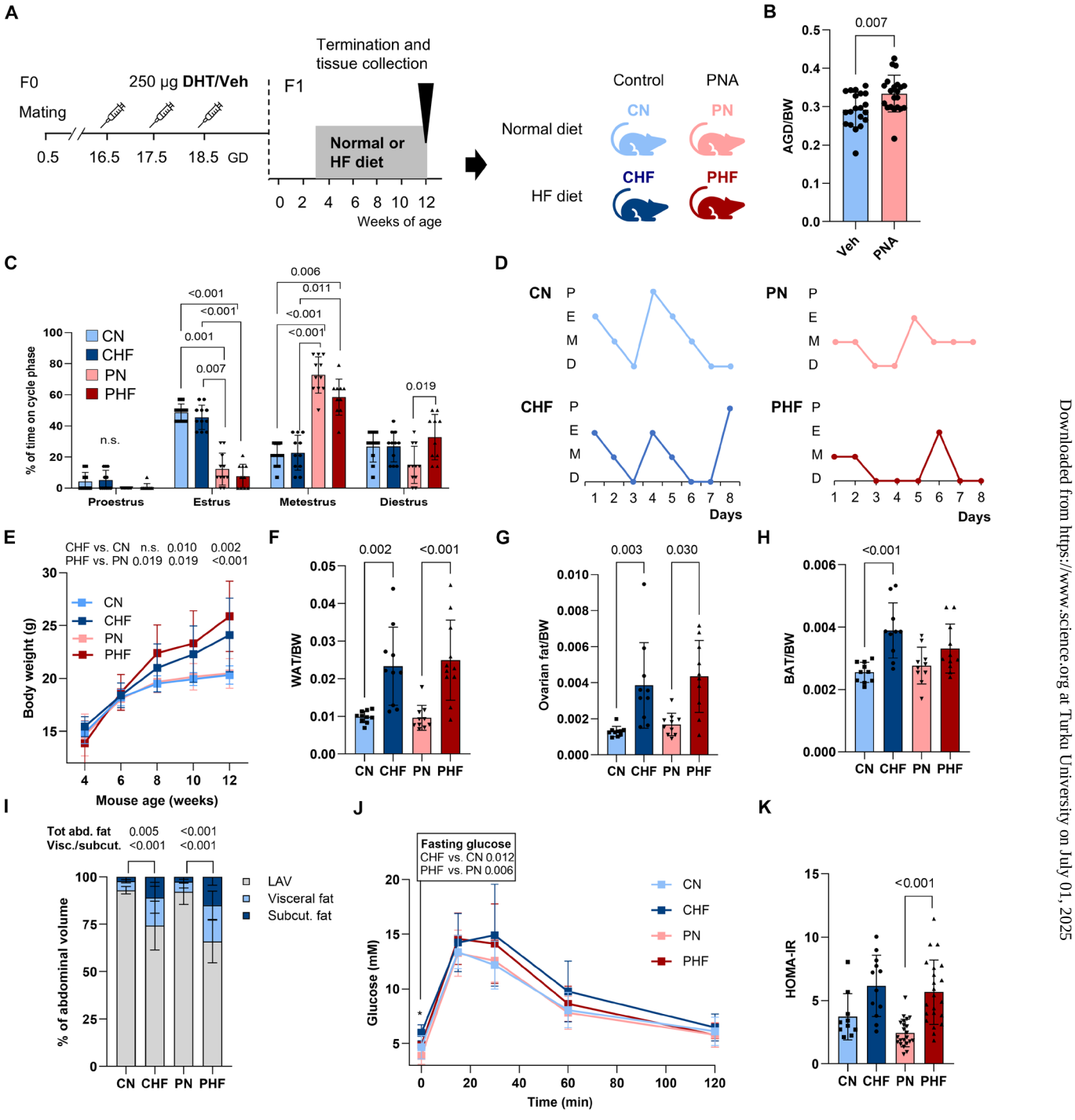

Fig. 1. Establishment of PCOS-like mice through PNA. (**A**) Experimental protocol. F1 are female offspring of the F0 generation. The four different experimental groups are CN, PN, CHF, and PHF. Veh, vehicle; GD, gestational days. (**B**) Anogenital distance (AGD) normalized to BW. $n \geq 20$ mice. (**C**) Percentage of time spent in different phases of the estrous cycle during a 21-day daily assessment. $n \geq 10$ mice. n.s., not significant. (**D**) Representative estrous cycles. Representative data of $n \geq 10$ mice. P, proestrus; E, estrus; M, metestrus; D, diestrus. (**E**) BW development from 4 weeks onward. Comparisons between diet groups per time point are shown. $n \geq 11$ mice. (**F** to **H**) Wet weights of white adipose tissue (WAT) (F), ovarian fat (G), and brown adipose tissue (BAT) (H) normalized to BW. Comparisons between diet groups are shown. $n \geq 10$ mice. (**I**) Microcomputed tomography (microCT) analysis of the proportion of lean abdominal (abd.) volume (LAV) and visceral (visc.) and subcutaneous (subcut.) fat volumes of the abdomen. Comparisons of total abdominal fat proportion or proportion of visceral versus subcutaneous fat between diet groups are shown. $n \geq 10$ mice. (**J**) Blood serum glucose concentration at fasting (0 min) and during glucose tolerance (GT) test. $n \geq 11$ mice. (**K**) Homeostatic model assessment for insulin resistance (HOMA-IR) score. $n \geq 10$ mice. Student's *t* test (B), one-way analysis of variance (ANOVA) or Kruskal-Wallis test [(C) to (I) and (K)], or repeated-measures two-way ANOVA (J). Data are presented as mean ± SD. Data points represent individual mice.

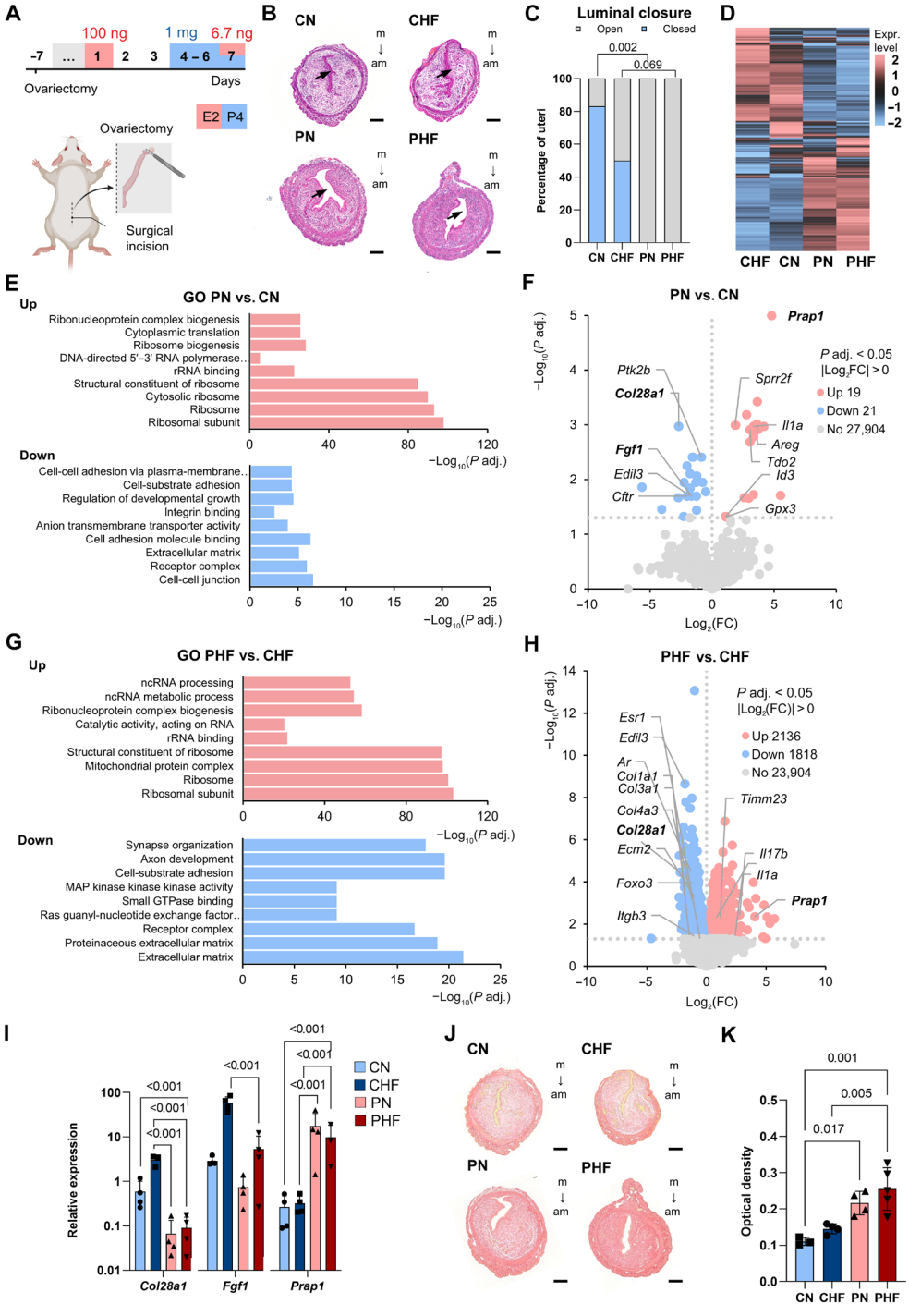

Fig. 2. PNA mice show failed luminal closure and abnormal extracellular matrix deposition during the WOI. (**A**) Experimental protocol for the induction of the WOI state. Created in BioRender. Arffman, R. (2025 https://BioRender.com/5r79jge). E2, estrogen; P4, progesterone. (**B**) Representative images of hematoxylin and eosin (H&E)–stained cross sections of the uteri during the WOI. Arrows indicate uterine lumen. Scale bars, 200 μm. $n = 9$ mice. m, mesometrial; am, anti-mesometrial. (**C**) Percentage of uteri with closed versus open lumen per group. $n = 9$ mice. (**D**) Hierarchical clustering of samples based on log ratio fold change (FC) of gene expression. Red = up-regulated genes; blue = down-regulated genes. $n = 4$ mice. Expr., expression. (**E** and **G**) Top nine increased (up) or decreased (down) Gene Ontology (GO) pathways in PN versus CN (E) or PHF versus CHF groups (G). $n = 4$ mice. rRNA, ribosomal RNA; ncRNA, noncoding RNA; MAP, mitogen-activated protein; GTPase, guanosine triphosphatase. (**F** and **H**) Volcano plots representing the significantly differentially expressed genes (DEGs) in uteri from PN versus CN (F) or PHF versus CHF groups (H). Red = up-regulated; blue = down-regulated. Genes in bold were validated with reverse transcription quantitative polymerase chain reaction (RT-qPCR). $n = 4$ mice. (**I**) RT-qPCR expression analysis of *Col28a*, *Fgf1*, and *Prap1*. $n = 4$ mice. (**J**) Representative images of picrosirius red staining of fixed uterine cross sections during the WOI. Scale bars, 200 μm. $n \geq 3$ mice. (**K**) Quantification of mean optical density (OD) of picrosirius red staining of the stroma. $n \geq 3$ mice. Chi-square test (C) or one-way ANOVA [(I) and (K)]. Data are presented as mean ± SD. Data points represent individual mice [(I) and (K)].

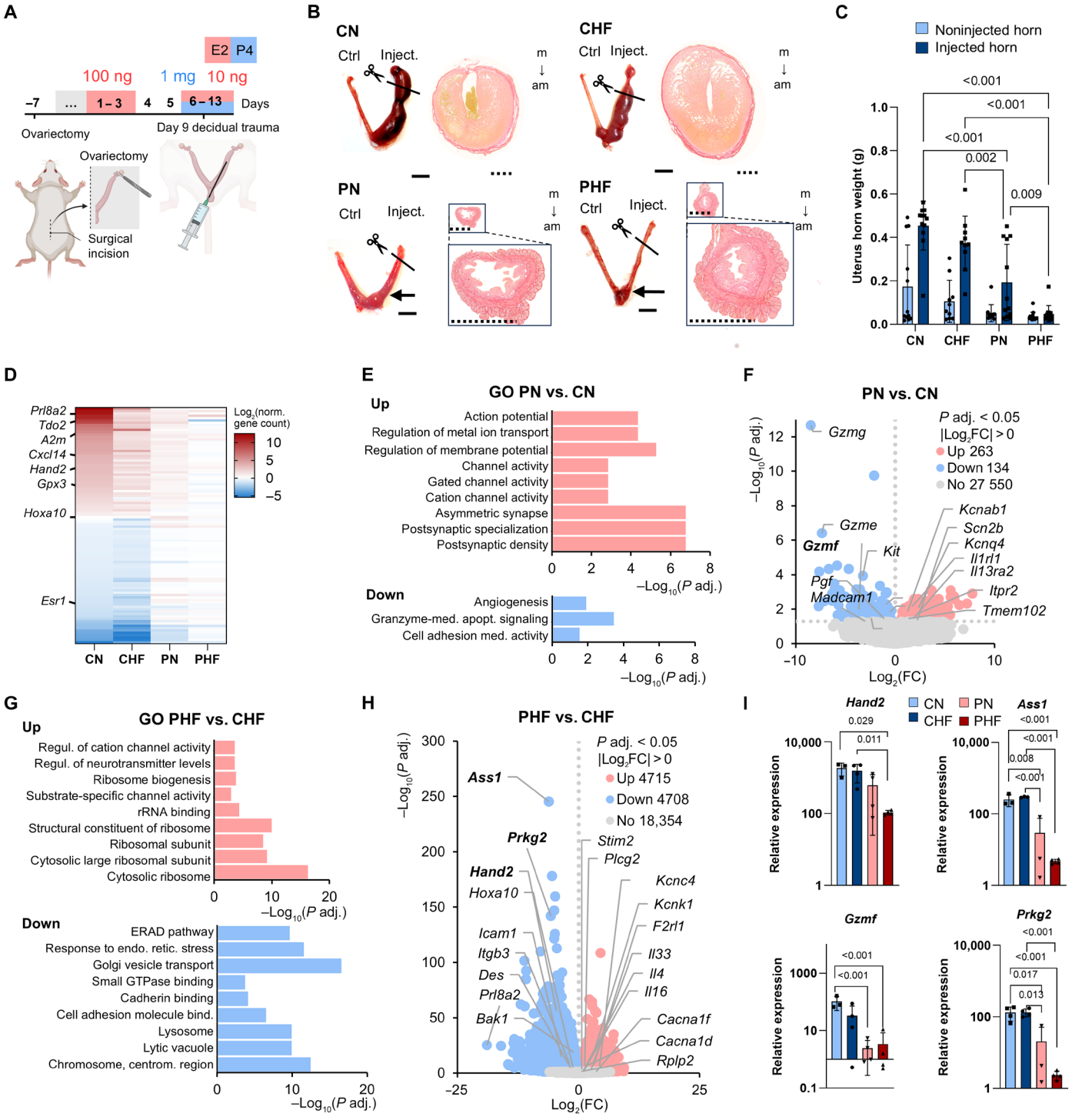

Fig. 3. PNA impairs the decidualization response in vivo. (**A**) Experimental protocol for the induction of endometrial decidualization. Created using BioRender. (**B**) Representative images of isolated uteri and picrosirius red–stained cross sections after decidualization treatment: Left horn is the noninjected control horn (Ctrl), and right horn is the injected horn (inject.). Line and scissors indicate the area for cross-sectioning. The arrow indicates the uterine fragment used for RNA-seq in PNA groups. Scale bars, 5 mm (full line) and 1 mm (dashed line). $n = 10$ (uteri) or 4 (cross sections) mice. (**C**) Wet weights of injected and noninjected uterine horns. $n \geq 10$ mice. (**D**) Heatmap of gene counts of top 100 markers of decidualization [list retrieved from Wang *et al.* (*17*)] in injected uterine horns normalized to noninjected horns. Norm., normalized. $n = 4$ mice. (**E** and **G**) Top nine increased (up) or decreased (down) GO pathways in injected uterine horns from PN versus CN groups (E) and PHF versus CHF groups (G). $n = 4$ mice. Granzyme-med. apopt., granzyme-mediated apoptotic; med, mediator; regul., regulation; ERAD, endoplasmic-reticulum-associated protein degradation; endo. retic., endoplasmic reticulum; bind., binding; centrom., centromere. (**F** and **H**) Volcano plots representing DEGs in injected uterine horns from PN versus CN (F) and PHF versus CHF (H) groups. $n = 4$ mice. (**I**) RT-qPCR expression analysis of *Hand2*, *Ass1*, *Gzmf*, and *Prkg2*. $n = 4$ mice. One-way ANOVA or Kruskal-Wallis test [(C) and (I)]. All data are presented as mean ± SD. Data points represent individual mice [(C) and (I)].

Next, via bulk RNA-seq transcriptomic analysis, the expression of the top 100 genes that are up- or down-regulated after decidualization [a list derived from a publicly available dataset (*17*)] was compared between the four experimental groups. While the injected horns of CN mice showed a typical decidualization gene signature characterized by up-regulation of *Prl8a2*, *Hand2*, and *Hoxa10*, and down-regulation of *Esr1*, this decidual gene signature was almost entirely absent in the PN and PHF groups (Fig. 3D). In accordance with this, no DEGs were found between the injected and noninjected uterine horns derived from the PN group, and only three DEGs (*Srp54b*, *Krt5*, and *Six1*) were detected in the PHF group, further confirming the strongly diminished decidualization response in these groups (fig. S3, A and B). The comparison of PN versus CN noninjected control uterine horns showed increased expression of inflammation-related genes (*Il13ra2* and *-1rl1*) and reduced pathway enrichment related to hormone action and insulin signaling (*Adipoq*, *Lep*, and *Agtr2*), the latter being linked to preeclampsia (fig. S3C) (*18*).

Further analysis of oil-injected uterine transcriptomes of PN versus CN groups revealed enriched pathways and DEGs related to ion homeostasis (*Kcnab1* and *-q4* and *Scn2b*), while pathways and DEGs related to angiogenesis (*Pgf*), granzyme-mediated apoptotic signaling (*Gzmg* and *-e*), and cell adhesion (*Madcam1*) were reduced (Fig. 3, E and F).

Regarding the effect of the HF diet, in accordance with the morphological observations, only two DEGs (*Rpl17* and *3830403N18Rik*) were found between CHF and CN injected uteri, indicating that the HF diet alone had a very limited impact on the endometrial decidualization capacity (fig. S3, D and E). On the other hand, similar to the WOI, the differential effect of the HF diet on PNA versus control mouse uteri was evident from the marked difference in the number of DEGs found between PHF and CHF injected uterine horns (9423) compared to PN versus CN injected horns (397). In PHF versus CHF injected uteri, pathways and DEGs related to inflammation (e.g., *Il4*, *Il33*, and *Il16*), ribosomal activity (*Rpl2*), and ion homeostasis (*Stim1*, *Kcn4*, and *Cacna1g*) were up-regulated. Conversely, down-regulated pathways and genes were associated with decidualization and uterine receptivity (*Ass1*, *Prkg2*, *Hand2*, *Hoxa10*, and *Prl8a2*), integrin binding (*Itgb3* and *Icam1*), and response to endoplasmic reticulum stress (*Bak1*) (Fig. 3, G and H). Last, the comparison of PHF and PN uteri showed the down-regulated pathways and DEGs related to endometrial function (*Tdo2* and *Hand2*) and the regulation of inflammatory response pathways (*Icam1* and *Il6ra*) (fig. S3, F and G).

The transcriptome data were validated using RT-qPCR analysis of *Hand2*, *Ass1*, *Gzmf*, and *Prkg2*, which supported the RNA-seq findings (Fig. 3I). Similar to the WOI, the overall expression of genes related to ion homeostasis was affected by PNA (fig. S3H).

PNA in mice results in lower pregnancy rate and fetal growth restriction

We next set to analyze uterine function during pregnancy, for which ovary-intact mice were mated and euthanized 16 days after the detection of a copulation plug. In the CN and CHF groups, all mice showed normal gestational weight gain, and all were pregnant after the 10-day mating period (Fig. 4, A and B). In contrast, 45% of PN and 38% of PHF mice did not follow normal gestational weight gain curves after the detection of a copulation plug and showed no gestation. Of these mice, 20% of PN and 50% of PHF mice showed sudden marked weight loss (>10% of BW) after initial weight gain, suggesting pregnancy loss (Fig. 4, A and B).

In mice that were still pregnant at embryonic day 16.5 (E16.5), litter size, the proportion of developmentally compromised embryos, and the number of reabsorption sites did not differ between the experimental groups (Fig. 4C). However, the embryonic weight of E16.5 embryos was reduced in PHF versus CHF mice, with a trend of further reduction in PHF versus PN mice ($P = 0.052$) (Fig. 4, D and E).

Next, serum steroid hormone concentrations were measured to assess gestational hyperandrogenism. The HF diet, but not PNA, significantly increased serum T and androstenedione (A4) concentrations at E16.5, and PNA mice exhibited lower serum P4 concentrations than controls (fig. S4A).

The analysis of isolated placental decidual transcriptomes at E16.5 from pregnancies with female offspring revealed increased inflammation in PN versus CN deciduae (increased expression of *Il1a*, *Il1b*, *Cxcl1*, *Cxcl2*, and *Cxcl5*), as well as in PHF versus CHF deciduae (increased expression of *Cxcl1*, *Cxcl16*, and *Il1a*) (Fig. 4, F to I). Furthermore, several pathways related to endoplasmic reticulum and cell cycle transition were reduced in PN versus CN placental deciduae. Notably, the expression of *Dkk1*, a glycoprotein secreted by decidual cells and central in trophoblast cell invasion and placentation (*19*), was reduced in PN versus CN female placental deciduae (Fig. 4, F and G). Apart from increased inflammation-related gene expression, the PHF versus CHF female placental deciduae showed increased expression of several genes involved in ion transport (*Slc8a2* and *Slc24a3*), while pathways and gene expression related to mitochondrial respiratory chain were reduced (*Ndufa13* and *Ndufas7* and cytochrome c oxidases *Cox5b*, *Cox8a*, and *Cox11*) (Fig. 4, H and I).

The HF diet alone caused differential pathway enrichment related to prolactin binding, endoplasmic reticulum, Ras, Rac, and nitric oxide signaling, the latter suggesting increased cellular stress (fig. S4B and dataset S1). Last, the transcriptomic effects of the HF diet in PNA groups were related to G protein–coupled receptors and chemokine activity (fig. S4C and dataset S1). The RT-qPCR expression analysis of inflammation-related targets supported RNA-seq findings (fig. S4D).

PNA mice show placental dysfunction and inflammation

We next assessed whether PNA and DIO affected the morphology of E16.5 placentas, but no differences in the size of the different layers, placental size, or placental thickness were found between PNA or HF diet versus control groups (Fig. 5, A and B, and fig. S5A). On the other hand, placental transcriptomes of PNA mice showed increased expression of pathways and genes related to the innate immune system function compared to controls, including chemokine and cytokine activity (*Cxcl10*, *Il1f9*, and *Ccl3*) and granulocyte and neutrophil migration (*Cxcl2*, *Il1b*, *Trem3*, and *Itgam*) (Fig. 5C and fig. S5B). In addition, the expression of genes regulating mitochondrial autophagy and mitochondrial outer membrane cell compartments (*Pink1*, *Bok*, and *Tomm7*) was down-regulated (Fig. 5C and fig. S5B).

The combination of the HF diet and PNA affected pathways and gene expression related to angiogenesis (increased *Lrg1*, *Aplnr*, *Dll4*, and *Mmp9*), oxygen binding (increased hemoglobin-related genes *Hbb-y*, *Hhba-x*, *Hhba-a1*, and *Hhb-a2*), and metabolic processes (such as secondary alcohol, cholesterol, sterol, and fatty acid metabolism) compared to CHF groups, all of which suggest placental

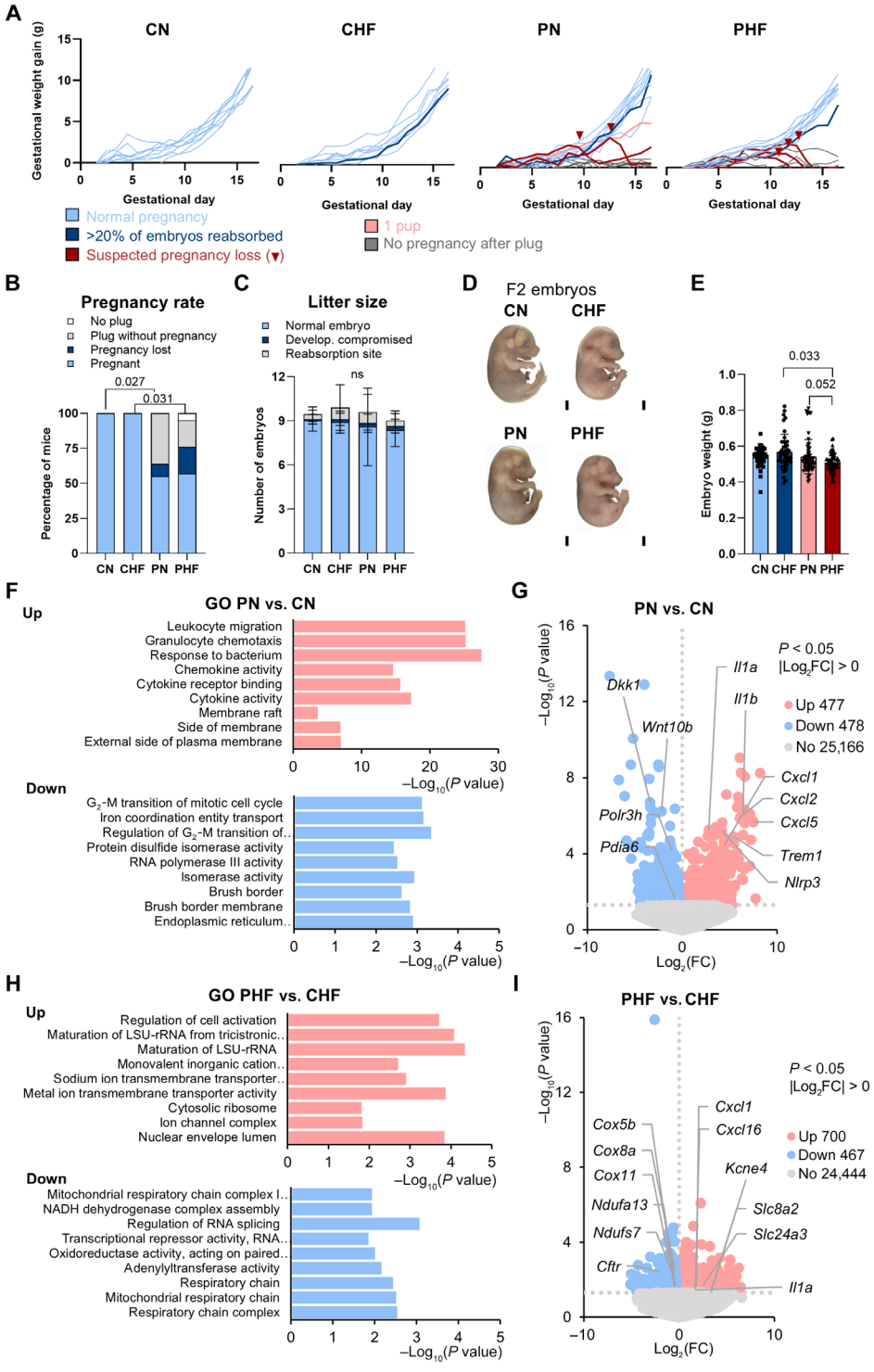

Fig. 4. PNA mice exhibit increased pregnancy loss, reduced embryo weight, and inflamed decidua. (**A**) Gestational weight gain follow-up of mice with a copulation plug [embryonic day 0.5 (E0.5)]. Colors refer to the assessment of pregnancy status upon termination at E16.5. The red triangle indicates the time point of suspected pregnancy loss. $n \geq 9$ mice. (**B**) Percentage of mice with no plug, a plug without subsequent pregnancy, suspected pregnancy loss, or normal pregnancy after a mating period of 10 days. $n \geq 9$ mice. (**C**) Number of normal, developmentally compromised, or reabsorbed embryos found per pregnant dam at E16.5. $n \geq 9$ mice. (**D**) Representative images of isolated F2 embryos at E16.5. Scale bars, 2 mm. $n = 63$ embryos. (**E**) Average F2 embryonic weight at E16.5, adjusted for embryo sex and litter size. $n = 63$ embryos. (**F** and **H**) Top nine increased (up) or decreased (down) GO pathways in deciduae from PN versus CN (F) or PHF versus CHF (H) groups. $n = 4$ mice. LSU, large subunit; NADH, reduced form of nicotinamide adenine dinucleotide (oxidized form). (**G** and **I**) Volcano plots representing DEGs in deciduae from PN versus CN (G) or PHF versus CHF (I) groups. $n = 4$ mice. Chi-square test [(B) and (C)] and pairwise comparisons of the linear mixed model estimated marginal means using the least significant difference post hoc test (E). All data are presented as mean ± SD. Data points represent individual embryos (E).

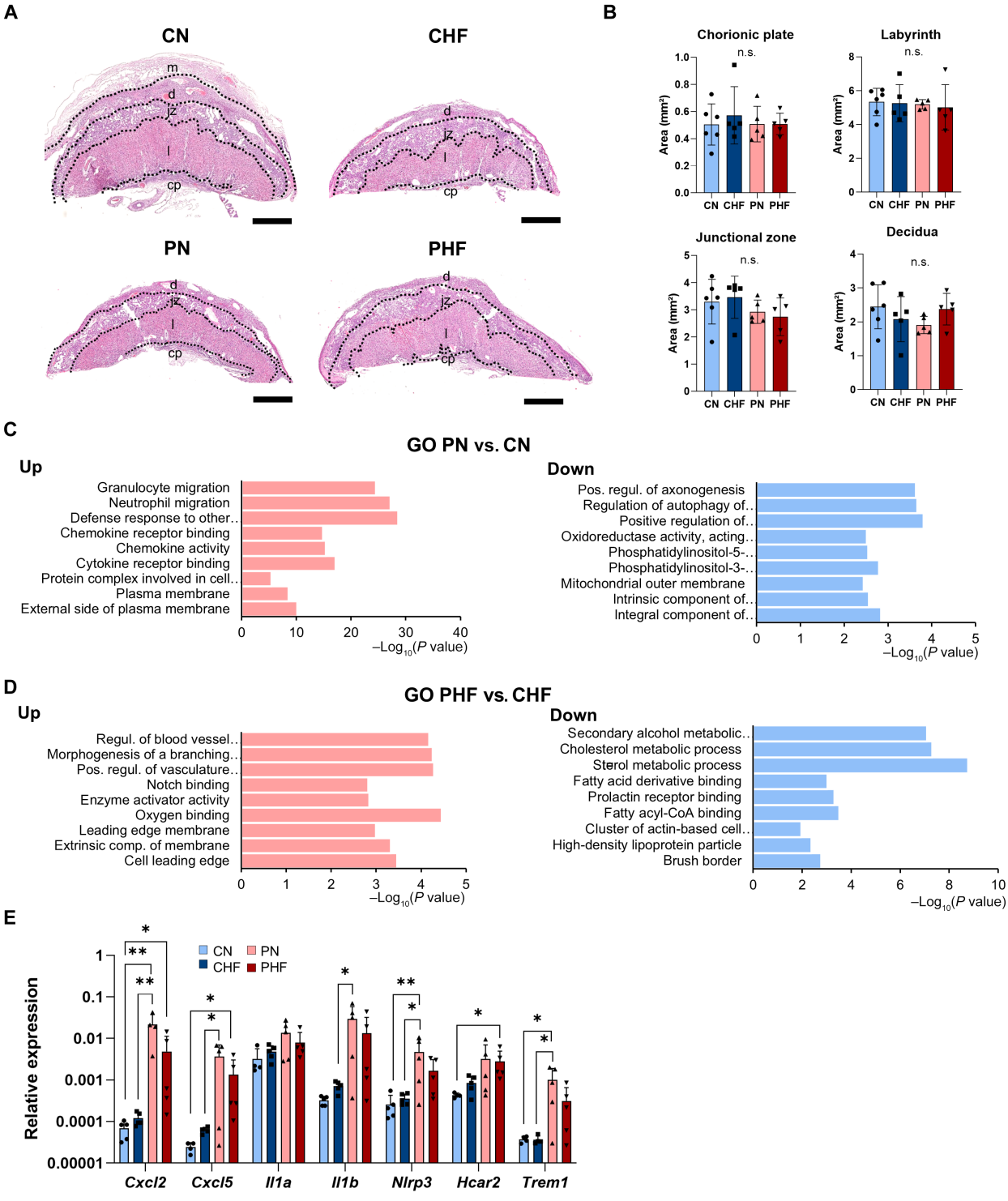

Fig. 5. PNA mice show increased placental inflammation at E16.5. (**A**) Representative images of H&E staining of fixed E16.5 placental cross sections. Placental layers indicated in the image: myometrium (m), decidua (d), junctional zone (jz), labyrinth (l), and chorionic plate (cp). Scale bars, 1 mm. $n = 5$ mice. (**B**) Size of the chorionic plate, labyrinth, junctional zone, and decidua. $n \geq 5$ mice. Two-way ANOVA. (**C** and **D**) Top nine increased (up) or decreased (down) GO pathways in E16.5 placentas from PN versus CN (C) or PHF versus CHF (D) mice. $n = 4$ mice. pos. regul., positive regulation; comp., component; CoA, coenzyme A. (**E**) RT-qPCR expression analysis of *Cxcl2*, *Cxcl5*, *Il1a*, *Il1b*, *Nlrp3*, *Hcar2*, and *Trem1* in placenta. $n = 5$ mice. All data are presented as mean ± SD. Data points represent individual mice.

blood vessel formation and function being affected (Fig. 5D and fig. S5C). The HF diet alone increased inflammation-related gene expression (*Ifi204*, *Gbp6*, *Oasl2*, and *Tgtp1*), prolactin receptor binding, and hormone activity (*Prl3d1*) and caused the down-regulation of several transmembrane transport activity pathways (*Slc16a9*, *Slc16a3*, and other *Slc* genes) (fig. S5D and dataset S2). Last, PHF versus PN comparison revealed increased gene expression and pathways linked to connective tissue development and cell-cell signaling (*Wnt4*, *Hoxa11*, and *Trpm4*) and a reduction of chromosomal and RNA regulation–related pathways and gene expression (*Esco2*, *Ccnb1*, and *Ndc80*) (fig. S5E and dataset S2).

The increased inflammation-related gene expression caused by PNA was further confirmed via RT-qPCR gene expression analysis of *Cxcl2*, *Cxcl5*, *Il1a*, *Il1b*, *Nlrp3*, *Hcar2*, and *Trem1* (Fig. 5E). Consistent with these findings, RNAscope in situ hybridization (ISH) demonstrated increased expression of *Nlrp3*, *Cxcl2*, and *Il1b*—genes typically associated with tissue inflammation (*20*–*22*)—in PN and PHF placentas. The increased expression was mainly located near blood vessels in decidua and the fetal membranes. In contrast, these targets were nearly undetectable in CN and CHF placentas (Fig. 6).

DISCUSSION

Despite the high prevalence and considerable economic burden of PCOS, its pathophysiology, particularly in relation to subfertility and pregnancy complications, remains inadequately understood. This knowledge gap hinders the development of effective fertility treatments and prepregnancy interventions. One of the key challenges has been understanding the specific role of the endometrium and the influence of metabolic factors in PCOS-related pregnancy complications. The individual impact of endometrial dysfunction on adverse pregnancy outcomes associated with PCOS has not been thoroughly elucidated, further complicating the search for targeted therapeutic solutions.

Previous studies have used PCOS-like mouse models to investigate PCOS-related traits and potential therapies (*10*, *23*, *24*). Among these, PNA has been widely recognized as the method of choice for inducing PCOS-like traits in rodent models, including characteristic ovarian morphology and anovulation (*25*). In this study, our aim was to explore the uterine function of the PNA model, specifically evaluating the individual and combined effects of PNA and DIO on the uterus, the placenta, and pregnancy development.

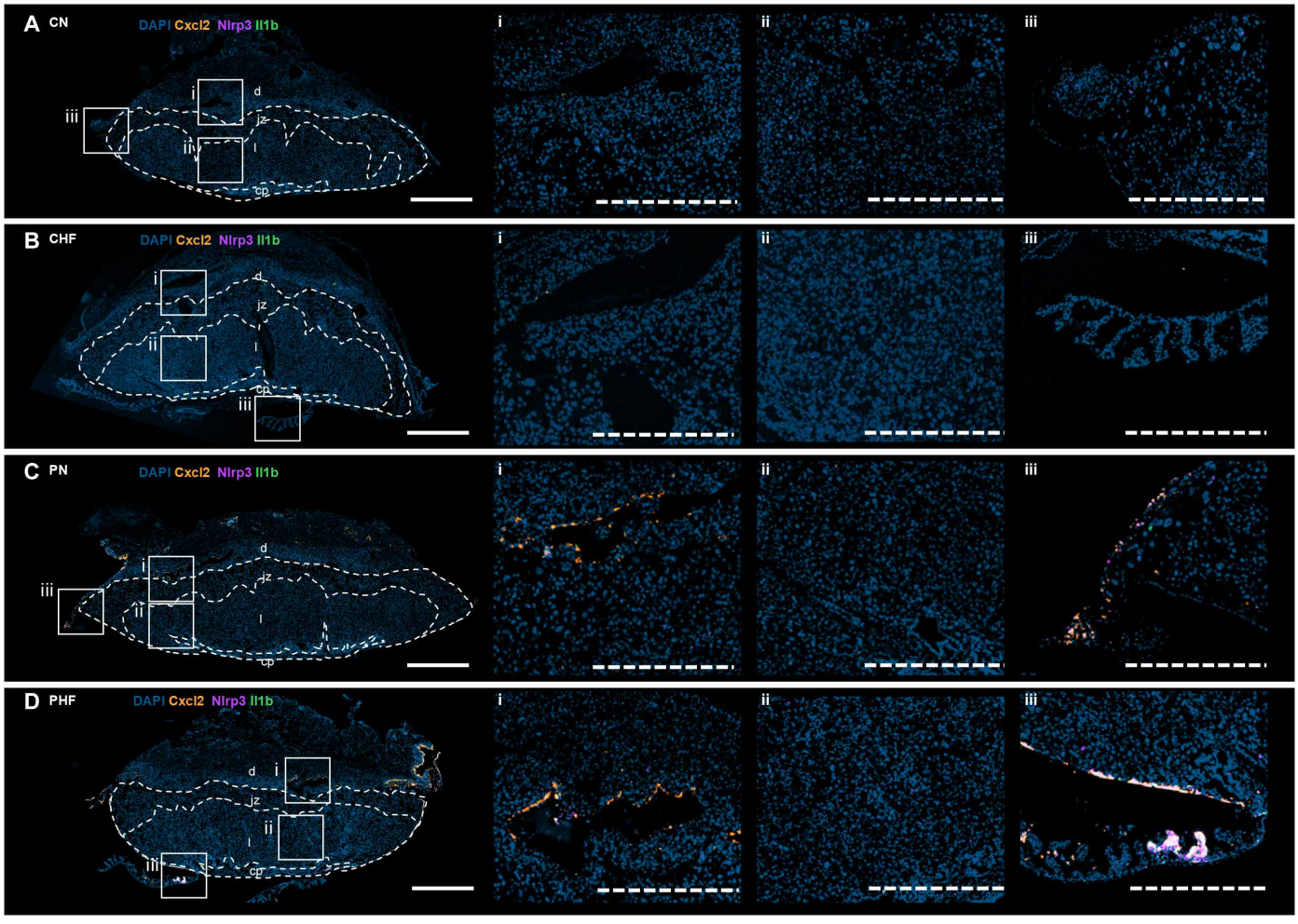

Fig. 6. ISH of inflammatory proteins in E16.5 placenta. (**A** to **D**) Representative images of RNAscope ISH of *Cxcl2* (orange), *Nlrp3* (purple), and *Il1b* (green) and in E16.5 placental cross sections. Boxed areas are magnified as indicated: i, decidual zone; ii, labyrinth; iii, fetal membranes. Scale bars, 1 mm (full line) and 500 μm (dashed line). $n = 5$ mice per group. DAPI, 4′,6-diamidino-2-phenylindole.

Successful induction of the PCOS-like phenotype was confirmed by the presence of increased AGD and disrupted estrus cycles (*13*, *26*). Some (*27*, *28*) but not all studies (*12*) have reported increased serum T levels in PNA mice. We did not observe any biochemical signs of hyperandrogenism, a discrepancy that we attribute to different analysis methods and the small sample size used in this study. We therefore suggest that the PNA model represents the PCOS phenotype D (*29*), constituting women with PCOS without measurable hyperandrogenism. We also confirmed the impact of an HF diet on metabolic health, evidenced by increased weight gain and higher proportions of subcutaneous and visceral abdominal fat, both associated with metabolic disturbances and cardiovascular disease risk in humans (*30*). Some authors have reported impaired glucose tolerance (GT) and elevated HOMA-IR scores in PNA mice (*31*, *32*), whereas our study and others (*12*) found no PNA-specific effects on GT.

To address the potentially confounding effects of ovarian signaling on uterine function, we investigated uterine endometrial differentiation during the WOI and decidualization phases in ovariectomized mice with standardized sex hormone treatment. During the WOI, in mice, the luminal fluid volume is reduced [regulated by epithelial ion channels such as epithelial sodium channel (ENaC) and cystic fibrosis transmembrane conductance regulator (CFTR)], while P4-driven stromal edema facilitates luminal closure, allowing for close contact between the blastocyst and the endometrium (*33*, *34*). Here, our data uncover that PNA disrupts this critical process, resulting in the failure of luminal closure during the WOI. In addition, we observed that PNA leads to significantly impaired decidualization, consistent with previous findings from a dehydroepiandrosterone-induced prepubertal PCOS-like mouse model (*35*). These defects may be partially attributed to blunted P4 effects in PNA mice. P4 is essential for both luminal closure and the suppression of estrogen-induced endometrial proliferation during the WOI, as well as for the initiation of decidualization (*6*, *36*). To support this, pathway enrichment analyses revealed enhanced ribosome and RNA polymerase functions, suggesting sustained proliferation during the WOI in PNA mice. In addition, the altered expression of key P4-responsive genes, such as *Prap1* (during the WOI) (*37*) and *Hoxa10* and *Hand2* (during decidualization) (*36*) was found. Further in-depth analysis of differentially expressed P4-responsive genes [fig. S6, A and B; list derived from Rubel *et al.* (*38*)] in PNA mice reinforced the hypothesis of aberrant P4 signaling in these mice.

The morphological abnormalities observed during the WOI and decidualization phases were only apparent after artificial sex hormone priming, whereas intact, nonovariectomized mice exhibited normal uterine morphology. This suggests that the absence of the corpus luteum (CL) in ovariectomized mice may contribute to the observed endometrial dysfunction. In humans, the CL plays a critical role in natural menstrual cycles by secreting not only P4 but also other factors such as relaxin, vasoactive agents, and angiogenic substances, which may support optimal endometrial development and implantation (*39*). The similarly unfavorable effect of the absence of CL is observed in women undergoing frozen embryo transfer in supplemented artificial cycles generated with sex hormones during infertility treatments. In these cases, the absence of CL is linked to a higher risk of placenta-related adverse pregnancy outcomes, such as pregnancy-induced hypertension and preeclampsia (*40*, *41*).

Another noteworthy finding was related to ion homeostasis, which plays a key role in the establishment of pregnancy (*34*, *42*). Our results indicate that during the WOI, the overall expression of genes related to ion homeostasis and calcium signaling was reduced in PNA mice. Conversely, during the decidualization phase, there was a general increase in ion homeostasis–related gene expression compared to control mice, regardless of diet. These previously unreported findings suggest that PNA alters ion homeostasis during pregnancy; however, how these alterations in gene expression translate to functional differences warrants further detailed studies.

ECM reorganization is essential for establishing endometrial receptivity and regulating the endometrial decidualization process (*43*, *44*). In these regards, we found that PNA also affected the ECM, as both transcriptome and protein-level data demonstrated aberrant collagen content in the PNA uteri during WOI and decidualization phases. The complexity of the ECM balance was supported by some discrepancies between the methods applied, revealing reduced ECM-related gene expression but higher picrosirius red staining during the WOI. While uterine fibrosis in PCOS-like rodents has been previously described (*45*), it remains to be investigated whether abnormal ECM balance is a driving factor or a consequence of uterine dysfunction in PCOS.

We also aimed to investigate the dual effects of PNA and DIO on the PCOS uterus. By adding an HF diet from a young age, we mimicked early-onset metabolic dysfunction commonly observed in women with PCOS (*46*). The deleterious effects of obesity on uterine function, including impaired decidualization and reduced embryo implantation rates (*47*), have been widely described. Our study did not show the major negative effects of the HF diet alone on uterine morphology in the WOI or decidualization phase. However, gene expression was notably altered during the WOI, particularly genes related to glucose metabolism and mitochondrial function. Of interest was the up-regulation of the PI3K/AKT pathway in HF diet–exposed mice during the WOI. This pathway is a key player in energy metabolism in insulin-sensitive tissues (*48*), and its hyperactivity has been frequently observed in endometrial cancer, a well-known PCOS-related adverse health outcome (*49*, *50*). During decidualization, the HF diet exposure resulted in more pronounced transcriptomic changes in PNA groups than in controls. A notable finding was that the effect of the HF diet exposure was different for PNA mice compared to controls, with a greater number of DEGs identified in the PHF versus CHF comparison than in the PN versus CN comparison across multiple experiments. This may suggest that PNA mice are more susceptible to the detrimental effects of an HF diet, possibly due to underlying impairment in the uterine environment. Overall, our data support a dual-hit disease model, where both PNA and HF diets individually exert relatively mild effects, but their combination leads to an exacerbated impact. Bishop *et al.* (*51*) demonstrated that prepubertal exposure to testosterone or a Western-style diet (WSD) in rhesus macaques independently impaired fertility, with testosterone delaying conception and WSD reducing pregnancy rates. Combined exposure exacerbated these effects, leading to pregnancy loss, again demonstrating a dual-hit effect, consistent with our findings (*51*). Our findings also support the body mass index–independent risk for adverse endometrium- and placenta-related outcomes in women with PCOS, such as endometrial cancer and small for gestational age (*52*, *53*). It may be speculated that a longer

period of an HF diet and more extreme BW could have induced more pronounced effects on uterine function also in control mice (*54*).

Last, we investigated whether PNA disrupts placental transcriptome and embryonic development by investigating embryos at E16.5 when the placenta is fully developed, and maximal performance is required to support fetal growth for the remainder of gestation (*55*). Our data showed an overall reduced pregnancy rate and plausible pregnancy loss as indicated by sudden weight loss in pregnant mice in PNA groups. A recent study using a more hyperandrogenic mouse model with continuous DHT exposure also found increased midgestational pregnancy loss in a PNA mice model, while cotreatment with the AR inhibitor flutamide could prevent this phenotype (*56*). In contrast to an earlier study reporting a reduced litter size in PNA mice (*12*), we did not detect significant differences in litter size at E16.5. However, because our study did not include birth data at the end of gestation, these studies are not fully comparable. Furthermore, in the study by Risal *et al.* (*12*), PNA fetuses were subjected to the HF diet during their PNA gestation, in contrast to our study with postnatal onset of the HF diet.

We also observed a fetal growth restriction in E16.5 litters from the PHF group compared to the CHF group, which likely reflects impaired decidua formation and subsequent placental function. Previous studies have reported placental-related growth restriction in dams on HF diets (*57*) and women with PCOS (*58*), corroborated by reduced placental blood flow observed through Doppler ultrasound in affected women (*59*). To support this, our findings indicate a reduction in pathways related to mitochondrial function in PNA mice, alongside altered placental expression of angiogenesis and hemoglobin-related genes (in the PHF group). This suggests a compensatory mechanism for placental blood vessel formation in the PHF group. Furthermore, these results again support the hypothesis that an HF diet exerts differential effects on PNA versus non-PNA mice, with PNA mice exhibiting reduced adaptive capacity compared to their non-PNA counterparts. These insights highlight the complex interplay between maternal diet, prenatal androgen exposure, and embryonic development, warranting further investigation into their clinical implications.

We found that the placental and uterine tissues of PNA mice showed an increased inflammatory profile. Increased uterine inflammatory gene expression was found throughout all assessed time points, including the WOI and decidualization phases, and it was most pronounced in PHF mice. In E16.5 placentas, the ISH assay of inflammation markers *Cxcl2*, *Nlrp3*, and *Il1b* suggested that the inflammation was located in the fetal membranes and maternal decidual veins. In line with these results, PCOS has been considered a "low-grade inflammatory state," which also has been reported in PCOS pregnancies (*60*, *61*). As for clinical relevance, inflammation has been suggested to contribute to pregnancy complications such as preeclampsia and gestational diabetes in PCOS (*62*). Notably, consistent with the observed changes in ion homeostasis– and calcium signaling–related gene expression during the WOI and decidualization phases, Ampey *et al.* (*63*) demonstrated that tumor necrosis factor–α—a cytokine commonly elevated in preeclampsia—can disrupt physiological uterine vascular remodeling through calcium signaling–related mechanisms. Therefore, the heightened inflammatory state may plausibly impair calcium signaling and, in turn, compromise gestational health.

Caution is warranted when extrapolating insights gained from mouse models to humans. While notable differences exist between the female reproductive systems of humans and mice (*6*, *64*), the correlation of several findings in our animal model with existing human data underscores the validity of the PNA mouse model in investigating PCOS-related endometrial dysfunction. Furthermore, the comparable outcomes in a nonhuman primate model (*51*) reinforce the translational relevance of our study with regard to the clinical management of PCOS. Another consideration is the reliance on bulk RNA-seq of whole uteri, which precludes the precise attribution of the DEGs to specific uterine compartments. Although many of the identified DEGs are known to play roles in the endometrium, future studies using single-cell RNA-seq and other localization analysis will be essential to distinguish their expression within the endometrial and/or myometrial contexts.

This study has novelty value by describing uterine defects resulting from the combination of PNA and an HF diet, independent of ovarian function, supporting the concept of a dual effect where PNA induces uterine and placental dysfunction, which is then exacerbated by the metabolic stress of an HF diet. Although the data on natural pregnancies were not independent of ovarian function, we were able to see similar changes in nonpregnant and pregnant decidua and placenta, supporting the idea of uterine-specific effects. The insights gained from this study are in line with clinical findings seen in human PCOS endometrium and pregnancies and thus contribute to the understanding of subfertility, pregnancy complications, and uterine function in PCOS. The results also highlight the need for studies on prepregnancy health optimization in women with PCOS targeting obesity and hyperandrogenism.

MATERIALS AND METHODS

Ethics statement and animal housing conditions

The use of animals in this study was approved by the ethical review committee for animal experiments at the National Animal Experiment Board in Finland (ELLA) and the KU Leuven (Belgium). The project numbers are 38/2020 and P033/2021, respectively. We complied with all relevant ethical regulations. Male and female C57BL/6J mice (Charles River, Germany) were housed in a conventional nonbarrier facility under controlled conditions (12:12 hour light:dark cycle, 23° ± 2°C and 40 to 60% relative humidity) and received ad libitum food pellets and tap water.

Experimental design

To induce PNA, female mice (F0) were mated (presence of a vaginal copulation plug = E0.5), after which pregnant females were subcutaneously injected with 250 μg of DHT (A8380, Sigma-Aldrich) in sesame oil (S3547, Sigma-Aldrich) and 5% benzyl benzoate (B6630, Sigma-Aldrich) or vehicle solution daily during E16.5 to E18.5. Next, 3-week-old female pups (F1) received either normal chow (2018, Envigo, USA; 24% kcal from protein, 18% kcal from fat, and 58% kcal from carbohydrates) or an HF chow (a mix of TD.160556 and TD.0881, Envigo, USA; 14 or 14.7% kcal from protein, 59.5 or 44.6% kcal from fat, and 25.8 or 40.7% kcal from carbohydrates, respectively) until termination. The female F1 mice were weighted weekly starting at the age of 4 weeks. For validation of the model, mice were terminated at the age of 12 weeks during the metestrus phase, after which AGD was measured, and wet weights of white (subcutaneous and visceral) and brown (from the neck) adipose tissue and ovarian fat were recorded. Postmortem blood was collected,

and the blood was centrifuged (1000*g* for 15 min at 4°C) to collect serum, which was stored at −80°C until further processing (Fig. 1A).

Assessment of the estrous cycle

Estrous cyclicity was assessed by performing a daily vaginal lavage with 50 μl of Dulbecco's phosphate-buffered saline (DPBS; Gibco) and subsequent determination of the predominant cell type using a microscope (10× objective) as described in (*65*) for 21 consecutive days. Regularly cycling, irregularly cycling, and noncycling phenotypes were assigned as described by Abruzzese *et al.* (*66*). Briefly, regularly cycling mice were categorized as displaying all four stages of the estrous cycle within 4 to 6 days; irregularly cycling mice showed some vaginal smears in the estrous stage but further smears did not follow the progress of the cycle or the cycle duration of was >7 days; and noncycling mice had vaginal smears showing metestrus, diestrus, or a combination of both for 4 consecutive days.

X-ray microCT

Twelve-week-old mice were anesthetized with 2% isoflurane in 100% oxygen, followed by scanning with a dedicated in vivo microCT scanner (SkyScan 1278, Bruker microCT, Kontich, Belgium) with the following parameters: 50 μm isotropic voxel size, 65 kV source voltage combined with a 1-mm aluminum filter, 770 μA current, 30 ms exposure time, and three averaged images per rotation step of 0.7° over 220°, within 2.5 min acquisition time. Raw images were reconstructed using NRecon software with 10% beam hardening correction and a ring artifact correction of 3. For fat measurements, the dynamic range was set at 0 to 0.017. The analysis of reconstructed images was done with DataViewer and CTAn software (Bruker microCT). Whole abdominal fat volume and subcutaneous and visceral fat volume proportions were quantified in three dimensions based on thresholding. First, manual delineation of a volume of interest (VOI) from vertebrae L1 to L6 was done to delineate the abdomen, after which segmentation of different tissue types, i.e., fat versus lean body mass, was done after thresholding based on the specific tissue density in CTAn software (Bruker microCT). Specifically, total abdominal adipose tissue volume was quantified as the total fat volume after thresholding for fat tissue within the VOI covering the abdomen. The lean abdominal volume (LAV) of the abdomen was defined as whole abdominal volume ($pixel^3$) minus whole adipose tissue volume ($pixel^3$). Next, to quantify visceral adipose tissue volume, a VOI delineating the abdominal muscle was drawn manually. Within this region of interest, the visceral adipose tissue volume was quantified after density thresholding. Subcutaneous adipose tissue volume was defined as whole adipose tissue volume ($pixel^3$) minus visceral adipose tissue volume ($pixel^3$). All measurements were reported as the percentage of the total abdominal volume.

GT test

Thirteen-week-old mice were fasted for 6 hours, followed by oral gavage of glucose (1 g/kg). Blood glucose was measured at 0 min (i.e., fasting blood levels) via the hind limb, followed by sampling at 15, 30, 60, and 120 min via the tail vein. Glucose was determined using the Freestyle Lite glucometer (Abbott), and insulin was determined using the Ultra Sensitive Mouse Insulin ELISA Kit (Crystal Chem). Homeostatic model assessment for insulin resistance (HOMA-IR) was determined as follows: fasting serum glucose (millimolar) × fasting serum insulin (mU/liter)/14.1.

Ovariectomy and preparation of hormones

All interventions were performed using sterile instruments. Thirteen-week-old nulliparous mice were given a subcutaneous injection of buprenorphine (0.1 mg/kg; Vetergesic multidose, Ecuphar) in saline (0.9% NaCl Viaflo, Baxter) and were anesthetized using 2% isoflurane (Iso-Vet, Dechra Veterinary Products) in 100% oxygen. Before surgery, the region of the intervention was shaved and disinfected with iso-Betadine and 70% ethanol. The anesthetized mice were placed on a 37°C heating pad during surgery and placed near heating during recovery to prevent hypothermia. For the ovariectomy, a small midline incision was made in the skin of the lower back of anesthetized mice, followed by a small lateral incision in the peritoneum to expose the abdominal cavity. The ovary was exposed, after which the ovary and fallopian tube were separated from the uterus and removed, and the skin wound was closed with wound clips (World Precision Instruments). For hormone injections, stock solutions of E2 (1 mg/ml; E8875, Sigma-Aldrich) and P4 (1 g/ml; P0130, Sigma-Aldrich) were prepared in 95% ethanol and further diluted in sesame oil for subcutaneous injections (100 μl per injection).

Induction of WOI and endometrial decidualization

The protocols for the induction of the WOI state and endometrial decidualization were adapted from Monsivais *et al.* (*67*) and Zhang *et al.* (*16*), respectively. Briefly, 1 week after ovariectomy, to induce the WOI state, mice received subcutaneous injections of 100 ng of E2 on day 1, followed by 1 mg of P4 on days 4 to 7 and 6.7 ng of E2 on day 7. Uteri were harvested 15 hours after the final injection (Fig. 2A). To induce endometrial decidualization, 1 week after recovery, ovariectomized mice received injections of 100 ng of E2 on days 1 to 3 and 10 ng of E2 with 1 mg of P4 on days 6 to 13. On day 9, the decidual trauma was induced in one uterine horn by inserting a blunt needle in the vagina and uterus of anesthetized mice, injecting 25 μl of sesame oil into one uterine horn, and light scratching of the uterine lumen. The other horn was left untreated (internal control). Uteri were harvested 6 hours after the final hormone injection (Fig. 3A). For RNA-seq, one piece from the noninjected horn and another piece from the injected uterine horn were separately stored in RNAlater. From uteri with minimal decidualization response, the part of the uterine horn with the most obvious sign of decidualization was collected (Fig. 3A).

Mating experiments

The estrous cycle of 10-week-old F1 mice was followed for 2 weeks before mating for 10 days (one male with two females per cage). Pregnant mice (presence of a vaginal copulation plug = E0.5) were separated and weighted daily until termination at E16.5. Upon termination, uteri were isolated, and placentas, embryos, and blood were collected and processed (see above). The placenta and deciduae of female E16.5 embryos [as determined by external genitalia (*68*)] were stored in RNAlater. Time to plug, number of mice with a plug, number of pregnant mice, and litter size were recorded. Maternal weight gain, embryonic weight (corrected for litter size and embryo sex), and overall embryonic morphology at E16.5 were assessed. Suspected pregnancy loss was defined as a weight loss of ≥10% after the detection of a copulation plug.

Serum measurement with liquid chromatography–tandem mass spectrometry

Serum T, A4, E2, and P4 were measured using liquid chromatography–tandem mass spectrometry at the Department of Clinical Chemistry

in the Sahlgrenska University Hospital (Goteborg, Sweden) as described in (*69*). The lower limits of quantification were T: 5 pg/ml; A4: 5 pg/ml, E2: 0.5 pg/ml; and P4: 5 pg/ml. For measurements in the nonpregnant state, serum from five mice was pooled per group in each run due to limited individual sample volumes. A total of two runs were performed.

Tissue processing and staining

Uterine horns and placental halves were fixed in 4% paraformaldehyde (PFA; Thermo Fisher Scientific) in DPBS overnight at 4°C, followed by two washing steps for 5 and 10 min in DPBS and storage in 70% ethanol at 4°C. After embedding, 5-µm sections from the middle of the uterine horn or placenta were collected onto glass slides, baked at 55°C for 1 hour, and deparaffinized and rehydrated in xylene and decreasing concentrations of ethanol. For hematoxylin and eosin (H&E) staining, slides were stained with hematoxylin solution (gill no. 3, Prosan) for 2 min, followed by immersion in 1% HCl (in 70% ethanol) and in $LiCO_3$ (saturated in distilled water). The slides were stained with eosin (Prosan) for 2 min. For picrosirius red staining, the slides were stained in 0.1% direct red 80 solution (Sigma-Aldrich) for 45 min, followed by washing in 0.5% acetic acid for 5 min (glacial, Supelco). For Masson's trichrome staining, the Masson's trichrome staining kit (HT15, Sigma-Aldrich) was used. The slides were stained with Weigert's iron hematoxylin (10 min), Biebrich scarlet–acid fuchsin solution (15 min), phosphomolybdic and phosphotungstic acid solutions (20 min), aniline blue solution (7 min), and 1% acetic acid solution (3 min). The slides were rinsed in distilled water in between steps. The stained slides were dehydrated in increasing concentrations of ethanol, followed by mounting (Micromount, Leica Biosystems) and imaging with Zeiss Axio Imager (20×) or Leica SCN400 Slide Scanner (Leica Biosystems).

RNAscope ISH

ISH for *Cxcl2* (Mm-Cxcl2, catalog no. 437581), *Il1b* (Mm-Il1b, catalog no. 316891), and *Nlrp3* (Mm-Nlrp3, catalog no. 439571) was done on E16.5 placentas using the RNAscope Multiplex Fluorescent v2 kit (Advanced Cell Diagnostics, USA). ISH assays were carried out according to the manufacturer's instructions using PFA-fixed, paraffin-embedded samples. Hoechst 1:2000 was used for nuclear staining. Imaging was done using the Zeiss Axioscan 7 microscope slide scanner with constant gain and exposure times, and Zeiss ZEN Lite software was used for image processing.

Tissue morphology analysis

ImageJ was used for morphological analysis of H&E-stained sections. From the uteri, the thickness of the luminal epithelial cell layer and the size of the lumen and endometrial and myometrial compartments were measured. For quantification of collagens from picrosirius-stained uteri, after color deconvolution, the mean staining intensity was measured and transformed to OD = log (max intensity/mean intensity). For placental morphology analysis, the surface area and the thickness of each layer (chorionic plate, labyrinth, junctional zone, and decidua) were calculated from midline placental sections using ImageJ software. The myometrium was excluded from analyses.

RNA isolation and RT-qPCR

Tissues were stored in RNAlater (Thermo Fisher Scientific) at −80°C until processing. RNA extraction and deoxyribonuclease treatment were performed using the RNeasy Mini Kit (QIAGEN) according to the manufacturer's instructions. RNA quality and quantity were checked with DropSense 16 (Trinean). For RT-qPCR, cDNA was synthesized using the RevertAid First Strand cDNA Synthesis Kit (Thermo Fisher Scientific), followed by RT-qPCR using the StepOne Real-Time PCR system. Triplicate cDNA samples were used. Forward and reverse primers were designed using PrimerBank or National Center for Biotechnology Information (NCBI) Primer-BLAST. The primer sequences are listed in table S1. Glyceraldehyde-3-phosphate dehydrogenase (*Gapdh*) and tyrosine 3-monooxygenase/tryptophan 5-monooxygenase activation protein zeta (*Ywhaz*) were used as housekeeping genes for uteri. *Gapdh* and Actin β (*Actb*) were used as housekeeping genes for the placenta. Relative expression levels are shown as 2^{-dCt} (mean ± SD) where $dCt = Ct_{target\ gene} - Ct_{housekeeping\ gene}$.

Transcriptome analysis using RNA-seq

Isolated RNA was submitted to Novogene Europe for RNA-seq, where mRNA purification was done using poly-T oligo-attached magnetic beads, followed by fragmentation and first- and second-strand cDNA synthesis using random hexamer primers and 3′-uridine 5′-triphosphate or 3′-deoxythymidine 5′-triphosphate, respectively. Library check was done using Qubit real-time PCR (for quantification) and bioanalyzer (for size distribution detection). After cluster generation, the library preparations were sequenced using the Illumina NovaSeq 6000 platform, and paired-end reads were generated. Raw reads (FASTQ format) were processed with Novogene in-house protocols to remove reads containing adapters, reads containing poly-N, and low-quality reads from raw data. Cleaned reads were mapped to the reference genome [*Mus Musculus* (GRCm38/mm10)] using Hisat2 v2.0.5. featureCounts v1.5.0-p3 was used to count the number of reads mapped to each gene, and FPKM (expected number of fragments per kilobase of transcript sequence per million base pairs sequenced) was calculated. Differential expression analysis was performed using DESeq2 R package (1.20.0). The resulting *P* values were adjusted using Benjamini and Hochberg's approach for controlling the false discovery rate (*P* adj.). Unless stated otherwise, genes with *P* adj. ≤ 0.05 were assigned as differentially expressed. Lists of DEGs can be found in datasets S1 to S4. The clusterProfiler R package was used to test DEG ($P < 0.05$) enrichment in GO. The depicted top nine increased or decreased GO pathways present the top three affected pathways for biological process, molecular function, and cellular component. Unless stated otherwise, GO terms or pathways with *P* adj. ≤ 0.05 were considered significantly enriched.

Statistics

All data are presented as mean ± SD unless stated otherwise. Only the *P* values of significant differences were depicted in the figures. Data analysis was performed using GraphPad Prism 10. A minimum of three replicates per experiment was used. RT-qPCR data were tested for outliers using the following method: data points < Q1 − 1.5*interquartile range (IQR) or data points > Q3 + 1.5*IQR were considered outliers, where IQR = Q3 − Q1. Normality was assessed using Shapiro-Wilk's normality test. Differences between two groups were determined by two-tailed Student's *t* test or Mann-Whitney test (in case of nonnormally distributed data). Differences between more than two groups were determined by one-way analysis of variance (ANOVA) or Kruskal-Wallis test (in case of nonnormally

distributed data), and Tukey correction for multiple comparisons was applied. Differences in proportions were tested by the chi-square test or Fisher's exact test. Differences were considered statistically significant at P or P adj. < 0.05.

Supplementary Materials

The PDF file includes:
Figs. S1 to S6
Table S1
Legends for datasets S1 to S4

Other Supplementary Material for this manuscript includes the following:
Datasets S1 to S4

REFERENCES AND NOTES

1. E. Stener-Victorin, H. Teede, R. J. Norman, R. Legro, M. O. Goodarzi, A. Dokras, J. Laven, K. Hoeger, T. T. Piltonen, Polycystic ovary syndrome. *Nat. Rev. Dis. Primers* **10**, 27 (2024).
2. M. Bahri Khomami, S. Shorakae, S. Hashemi, C. L. Harrison, T. T. Piltonen, D. Romualdi, C. T. Tay, H. J. Teede, E. Vanky, A. Mousa, Systematic review and meta-analysis of pregnancy outcomes in women with polycystic ovary syndrome. *Nat. Commun.* **15**, 5591 (2024).
3. A. E. Joham, H. J. Teede, S. Ranasinha, S. Zoungas, J. Boyle, Prevalence of infertility and use of fertility treatment in women with polycystic ovary syndrome: Data from a large community-based cohort study. *J. Womens Health (Larchmt.)* **24**, 299–307 (2015).
4. S. Palomba, T. T. Piltonen, L. C. Giudice, Endometrial function in women with polycystic ovary syndrome: A comprehensive review. *Hum. Reprod. Update* **27**, 584–618 (2021).
5. S. M. Hawkins, M. M. Matzuk, The menstrual cycle: Basic biology, in *Annals of the New York Academy of Sciences* (Blackwell Publishing Inc., 2008), vol. 1135, pp. 10–18.
6. C. Y. Ramathal, I. C. Bagchi, R. N. Taylor, M. K. Bagchi, Endometrial decidualization: Of mice and men. *Semin. Reprod. Med.* **28**, 17–26 (2010).
7. M. Khatun, A. Meltsov, D. Lavogina, M. Loid, K. Kask, R. K. Arffman, H. R. Rossi, F. Lättekivi, K. Jääger, K. Krjutškov, A. Rinken, A. Salumets, T. T. Piltonen, Decidualized endometrial stromal cells present with altered androgen response in PCOS. *Sci. Rep.* **11**, 16287 (2021).
8. D. E. Broughton, K. H. Moley, Obesity and female infertility: Potential mediators of obesity's impact. *Fertil. Steril.* **107**, 840–847 (2017).
9. Y. M. Jeanes, S. Reeves, Metabolic consequences of obesity and insulin resistance in polycystic ovary syndrome: Diagnostic and methodological challenges. *Nutr. Res. Rev.* **30**, 97–105 (2017).
10. E. Stener-Victorin, V. Padmanabhan, K. A. Walters, R. E. Campbell, A. Benrick, P. Giacobini, D. A. Dumesic, D. H. Abbott, Animal models to understand the etiology and pathophysiology of polycystic ovary syndrome. *Endocr. Rev.* **41**, bnaa010 (2020).
11. S. R. Ferreira, A. A. Goyeneche, M. F. Heber, G. A. Abruzzese, C. M. Telleria, A. B. Motta, Prenatally androgenized female rats develop uterine hyperplasia when adult. *Mol. Cell. Endocrinol.* **499**, 110610 (2020).
12. S. Risal, Y. Pei, H. Lu, M. Manti, R. Fornes, H. P. Pui, Z. Zhao, J. Massart, C. Ohlsson, E. Lindgren, N. Crisosto, M. Maliqueo, B. Echiburú, A. Ladrón de Guevara, T. Sir-Petermann, H. Larsson, M. A. Rosenqvist, C. E. Cesta, A. Benrick, Q. Deng, E. Stener-Victorin, Prenatal androgen exposure and transgenerational susceptibility to polycystic ovary syndrome. *Nat. Med.* **25**, 1894–1904 (2019).
13. Y. Wu, G. Zhong, S. Chen, C. Zheng, D. Liao, M. Xie, Polycystic ovary syndrome is associated with anogenital distance, a marker of prenatal androgen exposure. *Hum. Reprod.* **32**, 937–943 (2017).
14. M. J. Illera, E. Cullinan, Y. Gui, L. Yuan, S. A. Beyler, B. A. Lessey, Blockade of the $\alpha_v\beta_3$ integrin adversely affects implantation in the mouse. *Biol. Reprod.* **62**, 1285–1290 (2000).
15. J. Long, C. S. Yang, J. L. He, X. Q. Liu, Y. Bin Ding, X. M. Chen, C. Tong, C. Peng, Y. X. Wang, R. F. Gao, FOXO3a is essential for murine endometrial decidualization through cell apoptosis during early pregnancy. *J. Cell. Physiol.* **234**, 4154–4166 (2019).
16. Y. Zhang, Z. Zhang, N. Kang, X. Sheng, Generation of a mouse artificial decidualization model with ovariectomy for endometrial decidualization research. *J. Vis. Exp.* e64278 (2022).
17. C. Wang, M. Zhao, W. Q. Zhang, M. Y. Huang, C. Zhu, J. P. He, J. L. Liu, Comparative analysis of mouse decidualization models at the molecular level. *Genes (Basel)* **11**, 935 (2020).
18. S. Plummer, C. Tower, P. Alonso, L. Morgan, P. Baker, F. Broughton-Pipkin, N. Kalsheker, Haplotypes of the angiotensin II receptor genes *AGTR1* and *AGTR2* in women with normotensive pregnancy and women with preeclampsia. *Hum. Mutat.* **24**, 14–20 (2004).
19. S. Peng, J. Li, C. Miao, L. Jia, Z. Hu, P. Zhao, J. Li, Y. Zhang, Q. Chen, E. Duan, Dickkopf-1 secreted by decidual cells promotes trophoblast cell invasion during murine placentation. *Reproduction* **135**, 367–375 (2008).
20. Y. Chen, X. Ye, G. Escames, W. Lei, X. Zhang, M. Li, T. Jing, Y. Yao, Z. Qiu, Z. Wang, D. Acuña-Castroviejo, Y. Yang, The NLRP3 inflammasome: Contributions to inflammation-related diseases. *Cell. Mol. Biol. Lett.* **28**, 51 (2023).
21. K. De Filippo, A. Dudeck, M. Hasenberg, E. Nye, N. Van Rooijen, K. Hartmann, M. Gunzer, A. Roers, N. Hogg, Mast cell and macrophage chemokines CXCL1/CXCL2 control the early stage of neutrophil recruitment during tissue inflammation. *Blood* **121**, 4930–4937 (2013).
22. F. Amjadi, Z. Zandieh, M. Mehdizadeh, M. Ajdary, A. Aghamajidi, E. Raoufi, R. Aflatoonian, Molecular signature of immunological mechanism behind impaired endometrial receptivity in polycystic ovarian syndrome. *Arch. Endocrinol. Metab.* **66**, 303–311 (2022).
23. N. Virtanen, U. Saarela, M. Karpale, R. K. Arffman, K. A. Mäkelä, K. H. Herzig, P. Koivunen, T. Piltonen, Roxadustat alleviates metabolic traits in letrozole-induced PCOS mice. *Biochem. Pharmacol.* **229**, 116522 (2024).
24. M. A. Sánchez-Garrido, V. Serrano-López, F. Ruiz-Pino, M. J. Vázquez, A. Rodríguez-Martín, E. Torres, I. Velasco, A. B. Rodríguez, E. Chicano-Gálvez, M. Mora-Ortiz, C. Ohlsson, M. Poutanen, L. Pinilla, F. Gaytán, J. D. Douros, B. Yang, T. D. Müller, R. D. DiMarchi, M. H. Tschöp, B. Finan, M. Tena-Sempere, Superior metabolic improvement of polycystic ovary syndrome traits after GLP1-based multi-agonist therapy. *Nat. Commun.* **15**, 8498 (2024).
25. J. Ren, G. Tan, X. Ren, W. Lu, Q. Peng, J. Tang, Y. Wang, B. Xie, M. Wang, The PNA mouse may be the best animal model of polycystic ovary syndrome. *Front. Endocrinol. (Lausanne)* **13**, 950105 (2022).
26. R. T. Mitchell, W. Mungall, C. McKinnell, R. M. Sharpe, L. Cruickshanks, L. Milne, L. B. Smith, Anogenital distance plasticity in adulthood: Implications for its use as a biomarker of fetal androgen action. *Endocrinology* **156**, 24–31 (2015).
27. A. M. Moore, M. Prescott, R. E. Campbell, Estradiol negative and positive feedback in a prenatal androgen-induced mouse model of polycystic ovarian syndrome. *Endocrinology* **154**, 796–806 (2013).
28. M. S. Silva, M. Prescott, R. E. Campbell, Ontogeny and reversal of brain circuit abnormalities in a preclinical model of PCOS. *JCI Insight* **3**, e99405 (2018).
29. B. C. J. M. Fauser, Revised 2003 consensus on diagnostic criteria and long-term health risks related to polycystic ovary syndrome. *Fertil. Steril.* **81**, 19–25 (2004).
30. Z. Xu, Y. Liu, C. Yan, R. Yang, L. Xu, Z. Guo, A. Yu, X. Cheng, L. Ma, C. Hu, G. Guglielmi, K. Hind, C. Hu, Original research: Measurement of visceral fat and abdominal obesity by single-frequency bioelectrical impedance and CT: A cross-sectional study. *BMJ Open* **11**, e048221 (2021).
31. A. V. Roland, C. S. Nunemaker, S. R. Keller, S. M. Moenter, Prenatal androgen exposure programs metabolic dysfunction in female mice. *J. Endocrinol.* **207**, 213 (2010).
32. Y. Zhou, M. Gong, Y. Lu, J. Chen, R. Ju, Prenatal androgen excess impairs beta-cell function by decreased sirtuin 3 expression. *J. Endocrinol.* **251**, 69–81 (2021).
33. R. Kobayashi, J. Terakawa, T. Omatsu, Y. Hengjan, T. Mizutani, Y. Ohmori, E. Hondo, The window of implantation is closed by estrogen via insulin-like growth factor 1 pathway. *J. Reprod. Infertil.* **18**, 231–241 (2017).
34. Y. C. Ruan, H. Chen, H. C. Chan, Ion channels in the endometrium: Regulation of endometrial receptivity and embryo implantation. *Hum. Reprod. Update* **20**, 517–529 (2014).
35. S. Y. Li, Z. Song, M. J. Song, J. W. Qin, M. L. Zhao, Z. M. Yang, Impaired receptivity and decidualization in DHEA-induced PCOS mice. *Sci. Rep.* **6**, 38134 (2016).
36. H. Wang, S. K. Dey, Roadmap to embryo implantation: Clues from mouse models. *Nat. Rev. Genet.* **7**, 185–199 (2006).
37. T. H. Kim, J.-W. Jeong, Proline-rich acidic protein 1 (PRAP1) is a target of ARID1A and PGR in the murine uterus. *Dev. Reprod.* **23**, 277–284 (2019).
38. C. A. Rubel, R. B. Lanz, R. Kommagani, H. L. Franco, J. P. Lydon, F. J. Demayo, Research resource: Genome-wide profiling of progesterone receptor binding in the mouse uterus. *Mol. Endocrinol.* **26**, 1428–1442 (2012).
39. M. M. Pereira, M. Mainigi, J. F. Strauss, Secretory products of the corpus luteum and preeclampsia. *Hum. Reprod. Update* **27**, 651–672 (2021).
40. Å. Magnusson, H. I. Hanevik, H. Laivuori, A. Loft, T. Piltonen, A. Pinborg, C. Bergh, Endometrial preparation protocols prior to frozen embryo transfer – Convenience or safety? *Reprod. Biomed. Online* **48**, 103587 (2024).
41. T. R. Zaat, E. B. Kostova, P. Korsen, M. G. Showell, F. Mol, M. Van Wely, Obstetric and neonatal outcomes after natural versus artificial cycle frozen embryo transfer and the role of luteal phase support: A systematic review and meta-analysis. *Hum. Reprod. Update* **29**, 634–654 (2023).
42. K. De Clercq, J. Vriens, Establishing life is a calcium-dependent TRiP: Transient receptor potential channels in reproduction. *Biochim.Biophys. Acta Mol. Cell Res.* **1865**, 1815–1829 (2018).
43. R. Favaro, P. A. Abrahamsohn, M. T. Zorn, Decidualization and endometrial extracellular matrix remodeling, in *The Guide to Investigation of Mouse Pregnancy* (Elsevier, ed. 1, 2014), pp. 125–142.
44. A. Savolainen, E. Kapiainen, V.-P. Ronkainen, V. Izzi, M. M. Matzuk, D. Monsivais, R. Prunskaite-Hyyryläinen, 3DMOUSEneST: A volumetric, label-free imaging method

evaluating embryo–uterine interaction and decidualization efficacy. *Development* **151**, dev202938 (2024).
45. Y. Zhou, H. Lan, Z. Dong, W. Li, B. Qian, Z. Zeng, W. He, J. Le Song, Rhamnocitrin attenuates ovarian fibrosis in rats with letrozole-induced experimental polycystic ovary syndrome. *Oxid. Med. Cell. Longev.* **2022**, 5558599 (2022).
46. E. Koivuaho, J. Laru, M. Ojaniemi, K. Puukka, J. Kettunen, J. S. Tapanainen, S. Franks, M. R. Järvelin, L. Morin-Papunen, S. Sebert, T. T. Piltonen, Age at adiposity rebound in childhood is associated with PCOS diagnosis and obesity in adulthood—Longitudinal analysis of BMI data from birth to age 46 in cases of PCOS. *Int. J. Obes. (Lond)* **43**, 1370–1379 (2019).
47. Z. Chen, E. Yiwen, J. Xiong, W. Li, X. Chen, N. Li, J. Long, C. Tong, J. He, F. Li, C. Zhang, Y. Wang, R. Gao, Dysregulated glycolysis underpins high-fat-associated endometrial decidualization impairment during early pregnancy in mice. *Biochim. Biophys. Acta Mol. Basis Dis.* **1869**, 166659 (2023).
48. M. S. Savova, L. V. Mihaylova, D. Tews, M. Wabitsch, M. I. Georgiev, Targeting PI3K/AKT signaling pathway in obesity. *Biomed. Pharmacother.* **159**, 114244 (2023).
49. R. E. Schmandt, D. A. Iglesias, N. N. Co, K. H. Lu, Understanding obesity and endometrial cancer risk: Opportunities for prevention. *Am. J. Obstet. Gynecol.* **205**, 518–525 (2011).
50. S. Kyo, K. Nakayama, Endometrial cancer as a metabolic disease with dysregulated PI3K signaling: Shedding light on novel therapeutic strategies. *Int. J. Mol. Sci.* **21**, 6073 (2020).
51. C. V. Bishop, R. L. Stouffer, D. L. Takahashi, E. C. Mishler, M. C. Wilcox, O. D. Slayden, C. A. True, Chronic hyperandrogenemia and western-style diet beginning at puberty reduces fertility and increases metabolic dysfunction during pregnancy in young adult, female macaques. *Hum. Reprod.* **33**, 694–705 (2018).
52. C. L. B. Frandsen, M. Gottschau, B. Nøhr, J. H. Viuff, T. Maltesen, S. K. Kjær, A. Jensen, P. F. Svendsen, Polycystic ovary syndrome and endometrial cancer risk: Results from a nationwide cohort study. *Am. J. Epidemiol.* **193**, 1399–1406 (2024).
53. M. Bahri Khomami, S. Hashemi, S. Shorakae, C. L. Harrison, T. T. Piltonen, D. Romualdi, C. T. Tay, A. Mousa, E. Vanky, H. J. Teede, Systematic review and meta-analysis of birth outcomes in women with polycystic ovary syndrome. *Nat. Commun.* **15**, 5591 (2024).
54. H. J. Skalski, A. R. Arendt, S. K. Harkins, M. MacLachlan, C. J. M. Corbett, R. W. Goy, A. Kapoor, G. Hostetter, R. L. Chandler, Key considerations for studying the effects of high-fat diet on the nulligravid mouse endometrium. *J. Endocr. Soc.* **8**, bvae104 (2024).
55. P. M. Coan, A. C. Ferguson-Smith, G. J. Burton, Developmental dynamics of the definitive mouse placenta assessed by stereology. *Biol. Reprod.* **70**, 1806–1813 (2004).
56. H. Lu, H. Jiang, C. Li, E. Derisoud, A. Zhao, G. Eriksson, E. Lindgren, H.-P. Pui, S. Risal, Y. Pei, T. Maxian, C. Ohlsson, A. Benrick, S. Haider, E. Stener-Victorin, Q. Deng, H. Lu, H. Jiang, C. Li, E. Derisoud, A. Zhao, G. Eriksson, E. Lindgren, H.-P. Pui, S. Risal, Y. Pei, E. Stener-Victorin, Q. Deng, T. Maxian, S. Haider, Dissecting the impact of maternal androgen exposure on developmental programming through targeting the androgen receptor. *Adv. Sci.* **11**, 2309429 (2024).
57. D. de Barros Mucci, L. C. Kusinski, P. Wilsmore, E. Loche, L. C. Pantaleão, T. J. Ashmore, H. L. Blackmore, D. S. Fernandez-Twinn, M. das G. T. do Carmo, S. E. Ozanne, Impact of maternal obesity on placental transcriptome and morphology associated with fetal growth restriction in mice. *Int. J. Obes. (Lond.)* **44**, 1087–1096 (2020).
58. S. Sadrzadeh, E. V. H. Hui, L. J. Schoonmade, R. C. Painter, C. B. Lambalk, Birthweight and PCOS: Systematic review and meta-analysis. *Hum. Reprod. Open* **2017**, hox010 (2017).
59. E. Sahin, M. Eraslan Sahin, M. M. Kirlangic, S. Kutuk, S. Daglıtuncezdi Cam, H. Can Ozdemir, E. Genc, Effects of different PCOS phenotypes on placental three-dimensional power Doppler indices and placental volume during the first trimester. *Placenta* **154**, 176–183 (2024).
60. R. K. Arffman, M. Saraswat, S. Joenväärä, M. Khatun, R. Agarwal, T. Tohmola, I. Sundström-Poromaa, R. Renkonen, T. T. Piltonen, Thromboinflammatory changes in plasma proteome of pregnant women with PCOS detected by quantitative label-free proteomics. *Sci. Rep.* **9**, 17578 (2019).
61. L. M. T. Stokkeland, G. F. Giskeødegård, M. Ryssdal, A. H. Jarmund, B. Steinkjer, T. S. Madssen, S. N. Stafne, S. Stridsklev, T. S. Løvvik, A. C. Iversen, E. Vanky, Changes in serum cytokines throughout pregnancy in women with polycystic ovary syndrome. *J. Clin. Endocrinol. Metab.* **107**, 39–52 (2022).
62. S. Palomba, A. Falbo, G. Chiossi, F. Orio, A. Tolino, A. Colao, G. B. La Sala, F. Zullo, Low-grade chronic inflammation in pregnant women with polycystic ovary syndrome: A prospective controlled clinical study. *J. Clin. Endocrinol. Metab.* **99**, 2942–2951 (2014).
63. A. C. Ampey, D. S. Boeldt, L. Clemente, M. A. Grummer, F. X. Yi, R. R. Magness, I. M. Bird, TNF-alpha inhibits pregnancy-adapted Ca^{2+} signaling in uterine artery endothelial cells. *Mol. Cell. Endocrinol.* **488**, 14–24 (2019).
64. F. Soncin, M. Khater, C. To, D. Pizzo, O. Farah, A. Wakeland, K. A. N. Rajan, K. K. Nelson, C. W. Chang, M. Moretto-Zita, D. R. Natale, L. C. Laurent, M. M. Parast, Comparative analysis of mouse and human placentae across gestation reveals species-specific regulators of placental development. *Development* **145**, dev156273 (2018).
65. A. F. Ajayi, R. E. Akhigbe, Staging of the estrous cycle and induction of estrus in experimental rodents: An update. *Fertil. Res. Pract.* **6**, 5 (2020).
66. G. A. Abruzzese, M. F. Heber, S. R. Ferreira, L. M. Velez, R. Reynoso, O. P. Pignataro, A. B. Motta, Prenatal hyperandrogenism induces alterations that affect liver lipid metabolism. *J. Endocrinol.* **230**, 67–79 (2016).
67. D. Monsivais, C. Clementi, J. Peng, M. M. Titus, J. P. Barrish, C. J. Creighton, J. P. Lydon, F. J. DeMayo, M. M. Matzuk, Uterine ALK3 is essential during the window of implantation. *Proc. Natl. Acad. Sci. U.S.A.* **113**, E387–E395 (2016).
68. L. B. Murdaugh, H. N. Mendoza-Romero, E. W. Fish, S. E. Parnell, A novel method for determining sex in late term gestational mice based on the external genitalia. *PLOS ONE* **13**, e0194767 (2018).
69. C. Ohlsson, M. Langenskiöld, K. Smidfelt, M. Poutanen, H. Ryberg, A. K. Norlén, J. Nordanstig, G. Bergström, Å. Tivesten, Low progesterone and low estradiol levels associate with abdominal aortic aneurysms in men. *J. Clin. Endocrinol. Metab.* **107**, e1413–e1425 (2022).

Acknowledgments: We thank the University of Oulu Biocentre Transgenic and Tissue Phenotyping Core Facility and Light Microscopy Core for the use of histological instruments and microscopes. We acknowledge the technical support from Novogene regarding RNA-seq. We are grateful for the help of laboratory technicians from the University of Oulu Medical Research Centre, KU Leuven Laboratory Animal Centre, and KU Leuven Research group for Implantation, Placentation and Pregnancy (POPPY). Part of the work was carried out with the support of The Oulu Laboratory Animal Centre Research Infrastructure, University of Oulu, Finland. We thank the Oulu University Faculty of Medicine Pathology Department for help with the immunohistochemical staining. In vivo imaging was performed at the Molecular Small Animal Imaging Centre (MoSAIC), a KU Leuven facility. Figure 2 was created using BioRender.com. **Funding:** This work was supported by the Horizon 2020 Marie-Curie MATER Innovative Training Network [813707 (T.T.P.)], the Oulu Scholarship Foundation Grant (L.L.), the Jusélius Foundation (T.T.P.), the Novo Nordisk Foundation [NNF21OC0070372 (T.T.P.)], the Research Council of Finland [315921, 321763, and 336449 (R.K.A. and T.T.P.)], and Fonds Wetenschappelijk Onderzoek [I006524N and G0A6719N (G.V.V. and J.V.)]. **Author contributions:** Conceptualization: L.L., E.H., R.K.A., R.P.-H., J.V., and T.T.P. Methodology: L.L., U.S., C.O., M.P., G.V.V., R.P.-H., J.V., and T.T.P. Validation: L.L., U.S., M.P., R.P.-H., J.V., and T.T.P. Formal analysis: L.L., M.M., E.H., N.O., R.P.-H., and T.T.P. Investigation: L.L., M.M., U.S., N.V., A.S., A.-K.N., C.O., G.V.V., R.K.A., R.P.-H., and J.V. Resources: A.-K.N., C.O., M.P., G.V.V., J.V., and T.T.P. Data curation: M.M., U.S., E.H., A.-K.N., and J.V. Writing—original draft: L.L., M.M., E.H., G.V.V., and T.T.P. Writing—review and editing: L.L., M.M., U.S., N.V., E.H., A.S., A.-K.N., C.O., M.P., G.V.V., R.K.A., R.P.-H., J.V., and T.T.P. Visualization: L.L., M.M., U.S., and R.P.-H. Supervision: G.V.V., R.K.A., R.P.-H., J.V., and T.T.P. Project administration: L.L., R.P.-H., and T.T.P. Funding acquisition: J.V. and T.T.P. **Competing interests:** The authors declare that they have no competing interests. **Data and materials availability:** RNA-seq data generated and/or analyzed during the current study are available in the NCBI GEO repository, accession number GSE278408. All other data needed to evaluate the conclusions in the paper are present in the paper and/or the Supplementary Materials.

Submitted 25 November 2024
Accepted 3 April 2025
Published 9 May 2025
10.1126/sciadv.adu3699